Statics and Dynamics of Symmetric Diblock Copolymers: A Molecular Dynamics Study

Michael Murat,[†,‡] Gary S. Grest,[*,§,||] and Kurt Kremer[†]

Max Planck Institut für Polymerforschung, Postfach 3148, 55021 Mainz, Germany, and Corporate Research Science Laboratories, Exxon Research and Engineering Company, Annandale, New Jersey 08801

Received September 24, 1998; Revised Manuscript Received November 9, 1998

ABSTRACT: Extensive molecular dynamics simulations are carried out to study static and dynamic properties of symmetric diblock copolymer melts, both in the disordered and in the lamellar phases. The lamellar phase is constructed using the natural lamellar spacing, determined from constant pressure simulations. The non-Gaussian character of the chains in the disordered phase is demonstrated and quantified. In the lamellar phase, the density profile of the separate blocks, as well as the interface thickness are determined as a function of chain length N and AB interaction parameter $\tilde{\epsilon}$, and compared with experiments and other theoretical results. Single chain and single block form factors indicate that the chains in the lamellar phase are distorted into stick-like objects. Our results in the disordered phase show a stronger dependence of the diffusion constant on the chain length than observed in previous simulations. Diffusion within the lamellar plane for systems with chains of length $N \leq 100$ monomers is found to be almost independent of $\tilde{\epsilon}$, in agreement with the predictions by Barrat and Fredrickson for Rouse chains. Diffusion perpendicular to the lamellae is exponentially suppressed with increasing $\tilde{\epsilon}$. Simulations with even longer chains (up to $N = 400$ monomers) indicate that, in the strong segregation regime, chain stretching lowers the entanglement density and shifts the tube motion characteristic of the chain dynamics in homogeneous melts of long chains toward much longer chains.

I. Introduction

Melts of AB diblock copolymers containing linear chains of incompatible A and B monomers (of length N_A and N_B respectively) joined chemically at one end exhibit many interesting structures depending upon their composition and temperatures.[1−5] Of these the simplest is the lamellar structure, formed by symmetric AB copolymers ($N_A = N_B$) at temperatures below the order−disorder transition (ODT) temperature. This structure contains alternating layers, such that each layer is richer in either A or B monomers.

Theoretical treatments of the diblock melts deal mainly with two limiting cases: the weak segregation limit, valid at temperatures near the ODT temperature, and strong segregation limit (SSL) at temperatures well below. For the weak segregation limit, Leibler[6] developed a mean field theory which predicts a phase transition from a disordered melt to an ordered phase, as the product χN crosses a critical value, which depends upon $f = N_A/N$, with $N = N_A + N_B$. Here χ is the temperature-dependent interaction parameter characterizing the AB incompatibility. For symmetric diblocks ($f = {}^1/_2$), the stable ordered phase has a lamellar structure. In mean field theory, the transition is second-order, occurring at $\chi N = \chi_{ODT} N \approx 10.5$. This theory assumes that the individual chains remain Gaussian, with their average squared radius of gyration satisfying the scaling behavior $\langle R_G^2 \rangle \propto N$ on both sides of the transition. As the transition temperature is approached from above, the compositional structure factor $S_c(q)$ is predicted to diverge at a characteristic wave vector $q^* \propto R_G^{-1}$. Just below the transition temperature, the lamellar structure has a sinusoidal composition variation of wave vector q^*. Inclusion of fluctuation effects, as done by Fredrickson and Helfand,[7] changes the order of the transition to first order and suppresses the divergence in $S_c(q^*)$. Fluctuations also give rise to an N-dependent correction to χ_{ODT}. Stepanow[8] has incorporated non-RPA corrections to this model and found changes in the results of Fredrickson and Helfand, including thermally induced chain stretching.

A different approach to include fluctuation effects has been developed by David and Schweizer[9] and Guenza and Schweizer.[10] This work is based on the integral equation polymer reference interaction site model (PRISM) developed by Schweizer and Curro.[11] One of the main differences from the Leibler, Fredrickson, and Helfand (LFH) approach is the underlying physical origin of the fluctuation corrections. The nonlinear feedback which changes the mean field second-order phase transition to first order is driven by higher order intramolecular interactions which are of single chain entropic origin in the LFH theory. In the PRISM theory the fluctuations are driven by connectivity induced finite size coupling of local and long wavelength fluctuations due to enthalpic intermolecular effects. This model has been shown to give a very good, consistent description of experimental data for the position of the ODT and the compositional structure factor $S_c(q)$.[10] Recently Guenza *et al.*[12] have developed a microscopic theory of self-diffusion for diblocks in the one-phase region based on polymer mode coupling theory. Model calculations indicate that as one approaches the ODT from above, suppression of the diffusion constant is enhanced as molecular weight increases.

Simulations[13−16] as well as experiments[17] have demonstrated the Gaussian assumption to be unfounded,

† Max Planck Institut für Polymerforschung.
‡ Permanent address: Soreq Nuclear Research Center, Yavne 81800, Israel.
§ Exxon Research and Engineering Company.
|| Premanent address: Sandia National Laboratory, Albuquerque, New Mexico 87185.

10.1021/ma981512p CCC: $18.00
Published on Web 01/20/1999

even at temperatures well above the ODT temperature. The average squared distance $\langle R_{AB}^2 \rangle$ between the centers of mass of the A and B blocks, scaled by its value for a homopolymer of identical length is found to increase with increasing χN,[13,14,16] while in the Gaussian approximation $R_{AB}^2(\chi,N)/R_{AB}^2(0,N)$ would be constant. Simulations and scattering experiments have also shown that q^* varies with the distance from the transition temperature, while the theory indicated it to be independent of χ.

The SSL theories[18−20] treat the diblock copolymer melts in the limit $\chi N \gg \chi_{ODT}N$. In this limit of a symmetric diblock, the two halves of the chain are well separated, with the lamellar layers containing only one type of monomer, except inside a small interface layer of width $\omega \propto \chi^{-1/2}$. The periodicity of the layers d_l is predicted to scale as $N^{2/3}\chi^{1/6}$, resulting from a competition between chain stretching that leads to a reduction of the AB interaction energy and chain coiling that maximizes the entropy.

In addition to these limiting theories, numerical self-consistent field theories[21−24] have also been applied for intermediate values of the χ parameter, resulting in theoretical phase diagrams, as well as concentration profiles and other equilibrium quantities of interest for lamellae and for a number of structures with other symmetries.

An important issue involving ordering in symmetric diblock melts is that of self-diffusion. One question of interest is how the diffusion is affected by the approach to the ODT in the disordered phase. Another one is how the lamellar ordering affects self diffusion. Barrat and Fredrickson[25] modeled the self-diffusion of a Rouse chain in a lamellar system as tracer diffusion of a chain in a periodic potential varying in one dimension, perpendicular to the lamellar planes. Close to the ODT, they applied perturbation theories, while far away from it, they used activated process theory. The intermediate regime was covered by numerical simulation of the Rouse model. They found that diffusion within lamellar planes is not affected by the periodic potential, while diffusion perpendicular to the lamellae is slowed down by an amount dependent upon the magnitude of the concentration fluctuations. While at temperatures slightly below the ODT the perpendicular diffusion constant $D_\perp$ is expected to be lower by about 40% compared to the parallel diffusion constant $D_\parallel$, it should decay exponentially with χN further away from ODT. Our preliminary simulations[26] confirm these predictions. Leibig and Fredrickson[27] studied the suppression of the diffusion constant of unentangled chains due to fluctuations in the disordered regime. Tang and Schweizer,[28] extending the polymer mode-coupling theory to diblocks, found that concentration fluctuations can significantly slow down diffusion near and below the ODT. Most experiments on unentangled chains have been performed on quenched, unoriented samples,[29−32] though there has been one recent study by Hamersky *et al.*[33] on a lamellar polystyrene-polyisoprene diblock which has been oriented by shear. All of these studies showed that there is no discontinuity for the (isotropic) diffusion constant at the ODT. Hamersky *et al.* showed that for temperatures below the ODT, the average D measured in unoriented quenched samples is comparable to $^2/_3 D_\parallel + {}^1/_3 D_\perp$, and $D_\perp/D_\parallel$ decreased rapidly as the temperature decreases.

For well entangled chains, both components of the diffusion constant have been measured for a number of poly(ethylenepropylene)−poly(ethylethylene) diblock copolymers oriented with the application of oscillatory shear.[34] These experiments[34,35] showed less anisotropy than predicted by the Rouse model. Near the ODT, $D_\parallel \simeq D_\perp$ while 70 K below the ODT, $D_\parallel \simeq 3D_\perp$. One explanation for the fact that $D_\perp/D_\parallel$ is so close to unity for entangled chains while it is much larger for unentangled chains is based on the tube model (reptation). If the motion of the chain is confined to a tube, then diffusion both in the plane and between the planes involve penetration of A monomers into the B-rich domain and vice versa. However in the strongly segregated regime, the activation barrier is expected to exceed the entropic barrier of an alternative block-retraction mechanism,[35] similar to the arm-retraction known from star polymers. This entropic barrier also gives rise to an exponential decay of both $D_\parallel$ and $D_\perp$ with increasing N, making an experimental distinction between the two mechanisms very difficult. However the reptation concept is based on the topological constraints imposed on a chain by its neighbor chains which are also random coils, sharing the very same volume. In the lamellar phase, chain orientation reduces the overlap and fewer chains share the very same volume. Thus one should expect at least a delayed crossover toward entanglement-dominated motion.

An alternative interpretation of these results has been put forward by Colby,[36] who suggests that diffusion perpendicular to the interface in a truly aligned sample should be considerably slower than in the parallel direction because of the free energy penalty of pulling an A block through the B domain and vice versa. He suggests that the samples of Lodge and Dalvi[35] are only partially ordered, with a sufficient number of defects that allow diffusion perpendicular to the lamellae without requiring A blocks in the B domain. Unfortunately, as we show below, the long time diffusion for entangled systems is too slow to be measured at the present time with computer simulations, so we cannot address this interesting aspect of the problem directly.

There have been some simulation studies of chain motion in the lamellar phase of diblock copolymers. Pan and Shaffer[37] carried out a lattice Monte Carlo simulation of diffusion in a strongly segregated symmetric ($\chi N = 45$) diblock system. The stated purpose of this work was to check whether the entanglement length N_e, as determined from the variation of the diffusion constant with the chain length, is different from N_e in a homopolymer melt. They argue that N_e remains the same. However, in view of our preliminary results,[26] which indicate a change in entanglement density with lamellar ordering, their argument is questionable. Pakula *et al.*[38] looked at relaxation of several single chain autocorrelation functions as a function of the temperature using the cooperative motion algorithm.[39] Hoffmann *et al.* carried out bond fluctuation model[40] simulations for both symmetric[16] and asymmetric[41] diblock copolymers. These simulations involved increasing χ of a disordered melt to above its critical value. In the time that they could follow the systems, the ordered systems (lamellar systems in case of symmetric diblock copolymers) were always polycrystalline. These studies focused on the scaling of both static and dynamic quantities with the chain length and AB interaction parameter. Haliloğlu *et al.*[42] calculated the mobility of chain ends and junction

points in lamellar systems composed of relatively short (N=20) chains.

Most of the previous simulation studies on symmetric diblock copolymers in the lamellar phase were carried out on lattices with predetermined dimensions.[37,38,42−45] Since the equilibrium dimensions of the lamellar system are not known *a priori*, these turn out to be incommensurate with the lattice dimensions, resulting in distortions of the lamellar structure in order to be compatible with the lattice used. In this work, we use a model developed by Grest *et al.*[14] that avoids this problem by carrying out simulations in the continuum at constant pressure (variable simulation cell dimensions) to determine the lamellar spacing for a system of given chain length and AB interaction energy. The resulting average lamellar spacing was then used in constant volume simulations for the study of diffusion behavior. Simulations in which the lamella spacing was intentionally chosen to be too large resulted in a distortion of the lamella structure so as to be more compatible with the correct lamellar spacing. To compare these results with those for disordered systems, we also simulated several disordered melts on both sides of the ODT.

In the following section we briefly describe the method and give details of the systems simulated. We then present our results for the collective and single chain equilibrium properties in section III. In section IV we present results for diffusion for both disordered and lamellar systems. In section V we discuss the reduction of entanglement effects in lamellar systems. Finally, in the last section, we summarize our main results.

II. Method and Methodology

We use a coarse grained bead-spring model similar to that used in our earlier studies of polymer melts and networks[46,47] and tethered chains.[48] In this model each chain consists of N beads, which we refer to as monomers, connected to form a linear chain. For diblocks, the model is generalized to include two types of polymer species, A and B, which are connected in a block of fN monomers of type A connected to a block of $(1 - f)N$ monomers of type B. Here we consider symmetric diblocks, $f = {}^1/_2$. The interaction potential $U_{IJ}(r)$ between two beads of types I, J = {A, B} separated by a distance r is taken as the repulsive part of a Lennard Jones 6:12 potential

$$U_{IJ}(r) = \begin{cases} 4\epsilon_{IJ}\left[\left(\frac{\sigma_{IJ}}{r}\right)^{12} - \left(\frac{\sigma_{IJ}}{r}\right)^{6} + \frac{1}{4}\right] & r \le r_c \\ 0 & r > r_c \end{cases} \quad (1)$$

where the cutoff distance $r_c = 2^{1/6}\sigma_{IJ}$. Here, ϵ_{IJ} and σ_{IJ} are, respectively, parameters fixing the energy and length scale for monomers of type I and J. Adjacent monomers along the chains are coupled through an anharmonic potential, $U^{ch}(r)$ given by

$$U^{ch}(r) = \begin{cases} -\frac{1}{2}kR_0^{\,2}\ln\left[1 - \left(\frac{r}{R_0}\right)^2\right] & r \le R_0 \\ \infty & r > R_0 \end{cases} \quad (2)$$

The parameters $k = 30\epsilon/\sigma^2$ and $R_0 = 1.5\sigma$ are chosen so that unphysical bond crossings and chain breaking are eliminated.[46−48] Because all the interactions are short ranged, the model is very efficient computationally. The details of the method have been described elsewhere.[46]

For symmetric copolymers, we set $\epsilon_{AA} = \epsilon_{BB} = \epsilon$, and $\epsilon_{AB}/\epsilon = 1 + \tilde{\epsilon}$. We also set $\sigma_{AA} = \sigma_{BB} = \sigma_{AB} = \sigma$, so that both types of monomers have the same molar volume. The length, energy and time scales in this model are determined by σ, ϵ, and $\tau = \sigma(m/\epsilon)^{1/2}$, with m being the mass of both types of monomers. The simulations were carried out at a temperature $T = \epsilon/k_B$. We set $k_BT = \epsilon = 1.0$ and $\sigma = 1.0$ throughout the paper.

The energy parameters are a special case of

$$\tilde{\epsilon} = \left[\epsilon_{AB} - \frac{1}{2}(\epsilon_{AA} + \epsilon_{BB})\right]/\epsilon \quad (3)$$

which represents the type of interactions used in simple lattice systems such as in Flory−Huggins theory. In ref 14, it was shown that this difference in the repulsive interaction strength between like and unlike monomers was sufficient to drive phase separation. Simply by varying $\tilde{\epsilon}$, while leaving the temperature T constant, one can induce a phase transition from a homogeneous blend to a system with two segregated coexisting phases and from a disordered diblock copolymer melt to one with lamellar order.[14] This approach also overcomes a problem inherent in experimental studies: namely, the dependence of the monomeric friction constant on the temperature. It is reminiscent of recent experiments by Gehlsen *et al.*[49] in which the phase separation of binary mixtures is studied as a function of the difference in deuterium content between two otherwise identical polymer species. This is an elegant way of studying phase transitions in polymer mixtures while circumventing the rather narrow temperature range of access between the glass transition and thermal degradation. For a symmetric polymer blend, the critical interaction strength $\tilde{\epsilon}_c = 3.4/N$.[14] For very small $\tilde{\epsilon}$, we found that $\chi \simeq 10\tilde{\epsilon}$. For $N\tilde{\epsilon} \gtrsim 1.0$, this simple relation begins to break down and χ increases more slowly with $\tilde{\epsilon}$. In many simulations,[13,16,37] it is explicitly assumed, we believe incorrectly, that $\chi \simeq z_{eff}\,\tilde{\epsilon}$ for all $\tilde{\epsilon}$, but this has not been independently verified. Here z_{eff} is the effective coordination number. For more discussions on this point see ref 14.

Our systems consist of M chains of length N. The dynamics are studied by solving Newton's equations of motion using a velocity−Verlet algorithm[50] with a time step $\Delta t = 0.013\tau$. The monomers are coupled weakly to a heat bath.[46,47] Systems of two different symmetries were considered, disordered and lamellar. In the former case, we studied cubic systems at density $\rho = 0.85\sigma^{-3}$ as described in refs 46 and 47 for a homopolymer melt ($\tilde{\epsilon} = 0$). The linear dimension L of the simulation cell is determined by $L = (N/\rho)^{1/3}$, where $N = MN$. The disordered systems simulated consisted of chains of length between 10 and 200, with the number of chains varying from 1600 for the shorter chains to 200 for the longest ones. A partial list of the systems simulated in the disordered regime is given in Table 1. For the static properties of the chain, some additional results from ref 14 are also included.

The lamellar state was constructed as described in ref 14. We took the lamellar planes to be perpendicular to the z axis. Since the lamellar spacing depends on the interaction strength $\tilde{\epsilon}$ and is not known *a priori*, we first ran a constant pressure simulation[14] at a pressure of $P = 5\epsilon\sigma^{-3}$ during which the dimensions of the simulation cell, parallel $L_{||}$ and perpendicular $L_\perp$ to the lamellar plane, were allowed to vary independently[51] for each value of $\tilde{\epsilon}$. This value of pressure was chosen, since it

Table 1. Simulation Details for a Disordered Melt of M Chains of Length N at a Monomer Density $\rho\sigma^3 = 0.85$ and Temperature $T = \epsilon/k_B$, in a Simulation Cell of Linear Size L[a]

M/N	$\tilde{\epsilon}$	L/σ	T_t/τ	$\langle R_G^2\rangle/\sigma^2$	$\langle R^2\rangle/\sigma^2$	$\langle R_{AB}^2\rangle/\sigma^2$	$6D\tau/\sigma^2$
100/10	0.0	10.6	1.30×10^5	2.2	13.0	–	4.3×10^{-2}
1600/10	1.0	26.2	2.60×10^4	2.2	13.4	5.3	3.9×10^{-2}
1600/10	2.0	26.2	1.30×10^4	2.3	13.9	5.5	3.45×10^{-2}
1600/10	3.0	26.2	2.60×10^4	2.3	14.2	5.6	3.1×10^{-2}
1600/10	4.0	26.2	1.30×10^4	2.4	14.5	5.8	2.85×10^{-2}
1600/10	6.0	26.2	1.30×10^4	2.4	15.1	6.0	2.55×10^{-2}
800/20	0.0	26.2	2.60×10^4	4.8	29.4	10.7	2.1×10^{-2}
800/20	0.5	26.2	3.90×10^4	5.0	30.0	11.2	1.9×10^{-2}
800/20	1.0	26.2	2.77×10^4	5.1	31.1	11.7	1.6×10^{-2}
800/20	1.5	26.2	1.30×10^4	5.3	32.5	12.4	1.45×10^{-2}
800/20	2.0	26.2	1.30×10^4	5.4	33.7	12.9	1.3×10^{-2}
800/20	3.0	26.2	2.60×10^4	5.7	36.2	14.0	1.0×10^{-2}
800/40	0.0	33.5	2.60×10^4	10.4	62.9	22.2	8.9×10^{-3}
800/40	0.5	33.5	5.20×10^4	10.9	66.1	24.4	7.2×10^{-3}
800/40	0.8	33.5	5.20×10^4	11.6	72.0	27.3	5.2×10^{-3}
800/40	1.0	33.5	5.20×10^4	12.1	76.0	29.1	4.4×10^{-3}
800/40	1.25	33.5	2.60×10^4	12.5	78.7	30.4	3.8×10^{-3}
800/40	3.0	33.5	6.50×10^4	13.3	85.9	33.7	3.2×10^{-3}
100/100	0.0	22.7	3.90×10^5	27.7	167.3	57.2	2.1×10^{-3}
200/100	0.15	28.7	6.50×10^5	28.0	168.9	60.0	2.0×10^{-3}
200/100	0.22	28.7	5.20×10^5	28.9	174.6	63.8	1.8×10^{-3}
200/100	0.3	28.7	6.50×10^5	30.7	187.8	71.0	1.3×10^{-3}
200/100	0.5	28.7	6.50×10^5	32.4	201.4	77.6	9.5×10^{-4}
200/100	1.0	28.7	2.48×10^5	36.5	233.3	92.2	8.0×10^{-4}
100/200	0.0	28.7	5.68×10^5	60.4	345.7	116.6	5.5×10^{-4}
100/200	1.0	28.7	3.95×10^5	68.2	396.9	158.2	2.6×10^{-4}

[a] Data were taken from runs of total time T_t after equilibration. All the results are for one continuous run for a single ensemble. Results for the mean square radius of gyration $\langle R_G^2\rangle$, the mean square end-to-end distance $\langle R^2\rangle$, the mean squared distance between the center of mass of the A and B segments $\langle R_{AB}^2\rangle$, and the diffusion constant D are given. Some of the data for $\tilde{\epsilon} = 0$ are from ref 62.

Table 2. Simulation Details for a Lamellar System of M Chains of Length N at a Monomer Density $\rho\sigma^3 = 0.85$ and Temperature $T = \epsilon/k_B$, in a Simulation Cell of Length $L_\perp$ Perpendicular to the Lamellar Plane and Cross-Sectional Area $L_\parallel^2$ [a]

M/N	$\tilde{\epsilon}$	$L_\perp/\sigma$	$L_\parallel/\sigma$	T_t/τ	$\langle R_G^2\rangle/\sigma^2$	$\langle R^2\rangle/\sigma^2$	$\langle R_{AB}^2\rangle/\sigma^2$	$D_\parallel\tau/\sigma^2$	$D_\perp\tau/\sigma^2$
800/40	0.9	57.3	25.8	5.80×10^4	11.9	74.4	28.4	9.5×10^{-4}	7.5×10^{-4}
800/40	1.0	57.6	25.7	1.04×10^5	12.2	77.0	29.5	9.1×10^{-4}	3.2×10^{-4}
800/40	1.2	58.0	25.6	1.17×10^5	12.4	78.3	30.2	9.2×10^{-4}	8.0×10^{-5}
800/40	1.4	61.8	24.8	7.93×10^4	13.1	83.2	32.2	9.2×10^{-4}	3.1×10^{-5}
800/40	3.0	68.9	23.5	7.44×10^4	14.1	91.6	36.1	8.8×10^{-4}	
800/40	9.0	74.8	22.6	5.20×10^4	15.0	98.9	39.4	8.0×10^{-4}	
200/100	0.3	44.1	23.1	6.65×10^5	31.8	197.9	74.6	2.1×10^{-4}	6.5×10^{-5}
200/100	0.5	49.5	21.8	6.50×10^5	35.2	222.5	87.3	2.1×10^{-4}	
200/100	1.0	53.1	21.1	6.50×10^5	37.2	238.0	94.5	2.1×10^{-4}	
200/100	3.6	64.7	19.1	6.50×10^5	40.9	266.4	107.5	1.3×10^{-4}	
200/100	9.0	68.8	18.5	3.90×10^5	45.6	302.0	123.8	1.6×10^{-4}	
200/200	0.2	73.9	25.2	8.83×10^5	75.8	479.9	189.0	1.9×10^{-5}	
200/200	1.0	87.3	24.4	6.50×10^5	85.0	540.0	225.0		
200/200	9.0	109.8	22.2	2.16×10^5	98.0	660.0	265.0		
200/400	0.1	120.5	27.9	2.34×10^5	148.5	943.8	366.8		
200/400	9.0	169.0	23.6	2.60×10^5	208.2	1396.2	579.5		

[a] The number of lamellar layers in the simulation cell are 4 for $N = 40$ systems and 2 for longer chains. Data were taken from runs of total time T_t after equilibration. All the results are for one continuous run for a single ensemble. Results for the mean square radius of gyration $\langle R_G^2\rangle$, the mean square end-to-end distance $\langle R^2\rangle$, the mean squared distance between the center of mass of the A and B segments $\langle R_{AB}^2\rangle$, and the parallel and perpendicular components of the diffusion constant D are given.

leads to an average density of $\rho \approx 0.85\sigma^3$. These runs allow the determination of the appropriate simulation cell dimension $L_\perp$ commensurate with the lamellar spacing d_l and of the corresponding $L_\parallel$. Usually within a $(1-2) \times 10^4\tau$, $L_\perp$ adjusts itself to the new $\tilde{\epsilon}$. The fluctuations in $L_\perp$ are about $\pm 2\sigma$, both before and after the change in $\tilde{\epsilon}$. The resulting lamellar spacing d_l was shown in ref 14 to scale very well with $N^{2/3}$ as predicted by self-consistent field (SCF) theory.[20,52,53]

The simulation cell dimensions were then fixed at an equilibrium configuration corresponding to $\tilde{\epsilon}$, and very long runs were carried out at constant volume to study the dynamics in the lamellar phase. The results presented here are for $M = 800$ chains of $N = 40$ and $M = 200$ chains of $N = 100$, 200, and 400. The lamellar systems contained 4 lamellar layers for $N = 40$ and 2 layers for $N \geq 100$.

Table 2 lists all the lamellar systems simulated. The total simulation time for each system is also listed. This time is much longer than any relaxation time of internal motions of individual chains (such as the autocorrelation time of radius of gyration fluctuations), and is long enough (for all $N = 40$ and 100 systems) to measure the diffusion constants. The dimensions of the simulation cells, as given by $L_\perp$ and $L_\parallel$ are determined from a constant pressure simulation, as described above. The chain dimensions, quantified by the mean squared radius of gyration $\langle R_G^2\rangle$, mean squared end-to-end distance $\langle R^2\rangle$, and the mean squared distance $\langle R_{AB}^2\rangle$ between the center of mass of the A and B sections are

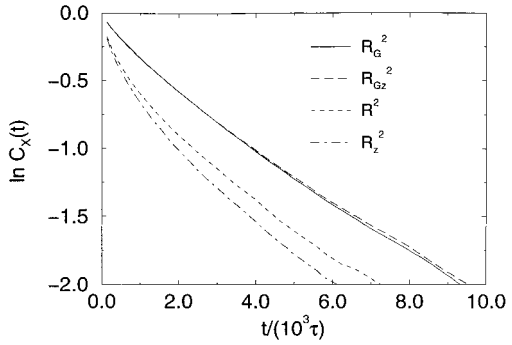

Figure 1. Autocorrelation function of the time dependence of various instantaneous chain dimensions, for a system of 200 chains of length $N = 100$ with $\tilde{\epsilon} = 1.0$, which is in the lamellar phase.

averaged over configurations sampled 10 000 time steps (130τ) apart, with the number of samples determined by the total length of the simulation. Also listed are the diffusion coefficients, measured as described later.

We measured the autocorrelation functions $C_X(t)$ of several single chain properties for the lamellar system. Results for $N = 100$, $\tilde{\epsilon} = 1.0$ are shown in Figure 1. $C_X(t)$ of a fluctuating variable $X(t)$ is given by

$$C_X(t) = \frac{\langle X(t)X(0)\rangle - \langle X\rangle^2}{\langle X^2\rangle - \langle X\rangle^2} \tag{4}$$

Here the brackets stand for an ensemble average over the chains, as well as over different starting times. In Figure 1, X is replaced by R_G^2, R^2 and their z contributions. $\langle R_G^2\rangle$ and $\langle R_{Gz}^2\rangle$ have typical relaxation times shorter than 5000τ. The end-to-end dimensions have even shorter autocorrelation times. Other $N = 100$ systems we studied exhibited similar relaxation times. For $N = 40$ typical autocorrelation times are of order 1000τ. These relaxation times are small compared to the total length of our simulations. Our results for chain diffusion (section IV) indicate that the time it takes a chain to diffuse its own radius of gyration is also very small compared to the total length of the simulations. Therefore, our simulations are indeed long enough to cover many equilibrium conformations of the chains.

We also simulated two additional systems which initially had lamellar symmetry, namely $N = 40$, $\tilde{\epsilon} = 0.8$ and $N = 100$, $\tilde{\epsilon} = 0.29$. The starting states of these were equilibrium configurations of system with $N = 40$, $\tilde{\epsilon} = 0.9$ and $N = 100$, $\tilde{\epsilon} = 0.3$, respectively. However, both these systems showed signs of melting after a few thousand τ, losing their lamellar structure. We could thus determine the lower limit of the $\tilde{\epsilon}_{ODT}$ for these two respective chain lengths as 0.8 and 0.29, consistent with the previous simulations[14] that indicated $\tilde{\epsilon}_{ODT} = 0.85 \pm 0.05$ and 0.28 ± 0.03, respectively. For $N \geq 200$, we do not have a good estimate for $\tilde{\epsilon}_{ODT}$. However the results for our simulation at $\tilde{\epsilon} = 0.2$ for $N = 200$ showed that this system is still lamellar but probably very close to the ODT. We thus expect $\tilde{\epsilon}_{ODT}$ for this chain length to be slightly less than 0.2.

III. Static Results

A. Structure of Disordered Systems. In the mean field model of Leibler the local structure of the copolymer melt is assumed to be indistinguishable from that of a homopolymer blend. It has been clearly shown from both experiment[1,17,54,55] and simulation[13,16] that, even

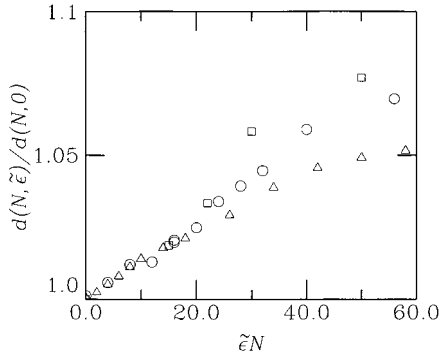

Figure 2. Ratio $d(N,\tilde{\epsilon})/d(N,0)$, where $d = \langle R_{AB}^2\rangle^{1/2}/\langle R_G^2\rangle^{1/2}$, vs the scaled interaction strength $\tilde{\epsilon}N$. Curves are for symmetric diblock copolymers of total length $N = 20$ (△), 40 (○), and 100 (□).

far above the ODT, the chains are locally stretched and show significant deviations from a Gaussian behavior. One direct way to see this effect is to measure the ratio d of the average distance between the centers of mass of the A and B blocks R_{AB}, to the radius of gyration R_G of the entire chain.[13] For a Gaussian chain, d is independent of N and is equal to $\sqrt{2}$.[13] For diblock copolymers however, d depends on N. This dependence is presented in Figure 2 where the increase of $d(N)$ with $\tilde{\epsilon}N$ clearly indicates a non-Gaussian behavior of the chains. The range of $\tilde{\epsilon}N$ covers and extends beyond the ODT. Because the relaxation time becomes very long near the transition, we find significant "supercooling" at large $\tilde{\epsilon}N$ of the disordered phase into the ordered regime. These supercooled states are clearly not in equilibrium and may explain why the results for different N separate for large $\tilde{\epsilon}N$ in Figure 2.

Further evidence for non-Gaussian behavior is found from the characteristic length scale of the fluctuations in $\psi = (\rho_A - \rho_B)/\rho$. This can be directly determined from the position of the peak in the collective structure factor $S_c(q)$. For a symmetric diblock copolymer, $S_c(q)$ is defined by

$$S_c(q) = \frac{1}{N}\sum_{ij} e^{i\mathbf{q}\cdot\mathbf{r}_{ij}}\langle\sigma(\mathbf{r}_i)\sigma(\mathbf{r}_j)\rangle \tag{5}$$

The sum is taken over all pairs in the system and $\mathbf{r}_{ij} = \mathbf{r}_i - \mathbf{r}_j$. The occupation factor $\sigma(\mathbf{r}) = -1$ for species A and 1 for species B. Because of the periodic boundary conditions only q values commensurate with the dimension of the simulation cell, $q_\alpha = (2\pi/L_\alpha)n$, where $n = 1, 2, \ldots$, are allowed. Figure 3 shows the results for spherically averaged structure factor $S_c(q)$ for $N = 40$ for six values of $\tilde{\epsilon}$. The solid line is a best fit to the data as discussed below. Note that as $\tilde{\epsilon}$ increases, the position of the first peak q^* shifts to smaller wave vectors and the height of the peak increases.

For symmetric diblock copolymers, Leibler[6] has shown that within mean field theory, $S_c(q)$ has the explicit form

$$NS_L^{-1}(q) = F(qR_G) - 2\chi N \tag{6}$$

where

$$F(x) = \frac{x^4}{2}\left(\frac{x^2}{4} + e^{-x^2/2} - \frac{e^{-x^2}}{4} - \frac{3}{4}\right)^{-1} \tag{7}$$

For all values of χN, $S_c(q)$ attains its maximum value at $q^*R_G = 1.95$ and diverges at the ODT. Clearly from

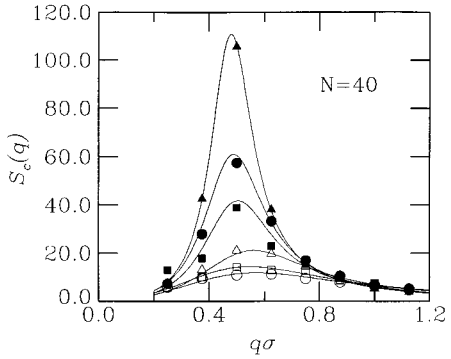

Figure 3. The spherically averaged compositional structure factor $S_c(q)$ vs q for $N = 40$ and $\tilde{\epsilon} = 0.10$ (○), 0.20 (□), 0.30 (△), 0.50 (■), 0.60 (●) and 0.80 (▲). The last value is close to the ODT, where $\tilde{\epsilon}_{ODT} = 0.85$. Also shown as solid lines are the curves fitted with eq 10.

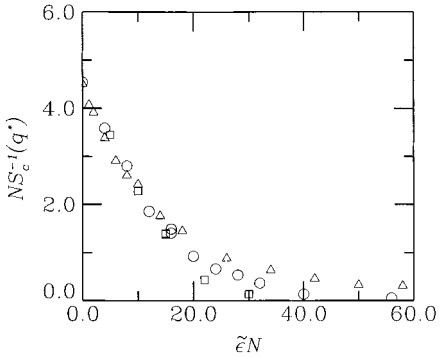

Figure 4. $NS_c^{-1}(q^*)$ vs $\tilde{\epsilon}N$ for $N = 20$ (△), 40 (○), and 100 (□).

Figure 3, the position of the peak decreases as $\tilde{\epsilon}$, and therefore χ, increases in contrast with the mean field prediction. Fredrickson and Helfand,[7] included the Hartree corrections and found that

$$NS_{FH}^{-1}(q) = NS_L^{-1}(q) + A[\tau_{FH}N]^{1/2} \tag{8}$$

where τ_{FH} is a solution of the equation

$$\tau_{FH} = NS_{FH}^{-1}(q^*) = F(q^*R_G) - 2\chi N + A[\tau_{FH}N]^{-1/2} \tag{9}$$

and A is a constant. The Hartree corrections introduce an explicit N dependence into the scaling form for $S_c(q)$. In this approximation, the order of the transition changes from second order to first. For finite N, the divergence in $S_c(q)$ at the ODT is also suppressed.

Since we can only calculate $S_c(q)$ at discrete sets of values of q, we follow Fried and Binder[13] and fit our data for the structure factor to a fitting function which has the same form as the predictions of Leibler[6] and Fredrickson and Helfand:[7]

$$NS_{fit}^{-1}(q) = \frac{1}{\alpha}[F(q\tilde{R}_G) - \delta] \tag{10}$$

Here $F(x)$ is given by eq 7. The three parameters α, δ, and $\tilde{R}_G = 1.95/q^*$ are treated as fitting parameters and obtained from a nonlinear least-squares fit to $S_c^{-1}(q)$.

Figure 3 shows the best fit to the structure factor for $N = 40$. In Figure 4, we show the value of the peak height $S_c^{-1}(q^*)$ vs $\tilde{\epsilon}N$ for three values of N. In agreement with earlier results of Fried and Binder,[13] the results scale very well with $\tilde{\epsilon}N$ as expected from the theoretical

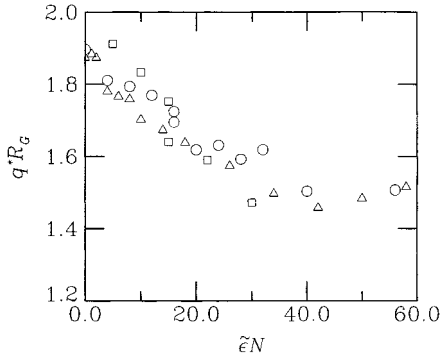

Figure 5. q^*R_G vs $\tilde{\epsilon}N$ for $N = 20$ (△), 40 (○), and 100 (□).

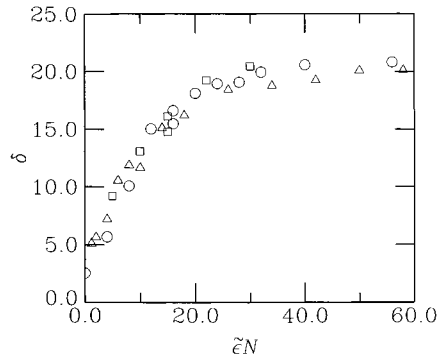

Figure 6. Fitting parameter δ, eq 10, vs $\tilde{\epsilon}N$ for $N = 20$ (△), 40 (○), and 100 (□).

predictions. A comparable plot vs $\tilde{\epsilon}$ does not scale, also in agreement with Fried and Binder. The deviations from the scaling for large $\tilde{\epsilon}N$ are for supercooled states with $\tilde{\epsilon} > \tilde{\epsilon}_{ODT}$. In mean field theory, $S_C^{-1}(q^*) \rightarrow 0$ linearly with $N\chi$ near the ODT. Extrapolating linearly the results shown in Figure 4 for $S_C^{-1}(q^*)$ to zero gives $N\tilde{\epsilon}_{ODT}^{MF} \simeq 20.0$. Since $N\chi_{ODT}^{MF} = 10.5$, this is another indication that $\chi \neq \tilde{\epsilon}$, contrary to what is often assumed. For $N = 40$, this gives $\tilde{\epsilon}_{ODT}^{MF} \simeq 0.5$ compared to the measured value of 0.85 ± 0.05.[14] For $N = 100$, the mean field result is 0.20 compared to 0.28 ± 0.03. As expected the mean field result becomes more reliable with increasing N.

The position of the local maximum q^* multiplied by the radius of gyration of the chain R_G is shown in Figure 5 for $N = 20$, 40, and 100. Note that the data scale reasonably well with $\tilde{\epsilon}N$ as suggested by Fried and Binder.[13] The large scatter is presumably due to the small system sizes. A plot of q^*R_G vs $\tilde{\epsilon}$ shows that if one had only the data for chains of length $N = 20$ and 40, as did Fried and Binder, it simply would not be possible to say whether the data scale better vs $\tilde{\epsilon}$ or $\tilde{\epsilon}N$. However, after including data for longer ($N = 100$) chains, we find clear indications that the data scale with $\tilde{\epsilon}N$, and not with $\tilde{\epsilon}$. Because of the relatively large scatter, we cannot rule out finite N corrections for these small chain lengths. For $\tilde{\epsilon} = 0$, $q^*R_G \simeq 1.95$, the value predicted in mean field theory[6] to within our uncertainty. However, it decreases rapidly as $\tilde{\epsilon}$ increases, reaching a value of about 1.6 at the ODT, slightly larger than the value 1.45 found by Fried and Binder.[13] There is no regime, even for small $\tilde{\epsilon}$, where q^*R_G is constant. The fitting parameter δ shows very good scaling with $\tilde{\epsilon}N$, as shown in Figure 6.

B. Structure in the Lamellar Phase. Figure 7 shows two snapshots of the simulation cell in two lamellar systems, each containing 200 chains of length

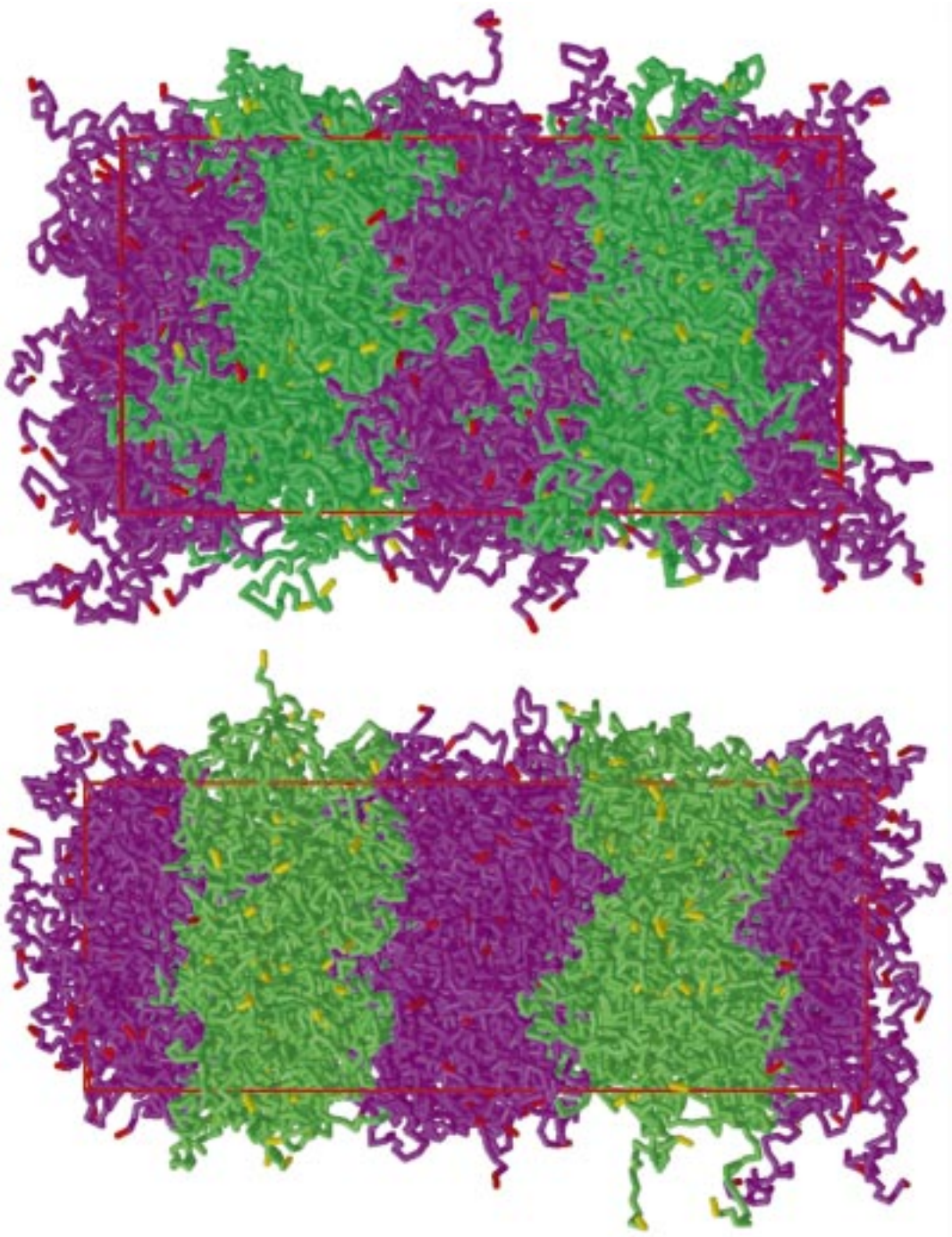

Figure 7. Top: snapshot of a system with 200 chains of length $N = 100$ for $\tilde{\epsilon} = 0.3$. The two types of the monomers are colored red and green, with the free ends of the green monomers shown in yellow. In the course of the simulation, monomers that leave the simulation box are folded back into the box through the use of periodic boundary conditions. Chains are plotted so that their centers of mass are inside the simulation cell. Monomers that extend beyond the cell are plotted outside the cell to emphasize the chain connectivity. The cell dimensions are $L_\perp = 44.1\sigma$ and $L_\parallel = 23.1\sigma$. Bottom: Snapshot for a system with the same chain length but at $\tilde{\epsilon} = 1.0$, which is much further from the ODT. For this system, $L_\perp = 53.1\sigma$ and $L_\parallel = 21.1\sigma$.

$N = 100$. Due to the periodic boundary conditions, chains are plotted so that their center of mass is within the simulations cells. Monomers that are out of the simulation cell are not folded back into the cell in order to show the connectivity. While the system with $\tilde{\epsilon} = 0.3$ (closest to the ODT) has a very broad interface, with monomers of one type interpenetrating into the domain of the other, the interface in the system with $\tilde{\epsilon} = 1.0$ is much better defined, with only few monomers penetrating the layer rich in the monomers of the other type.

It has been shown here in Figure 2, as well as in previous simulations,[13,16,56] that chains extend beyond their Gaussian dimension with increasing χN. In the lamellar phase they are expected to extend in a much more dramatic manner. The snapshots shown in Figure 7 demonstrate this extension qualitatively. For a more quantitative analysis, we show in Figure 8 the equilibrium lamellar spacing d_l scaled by $N^{2/3}$ for all the lamellar systems simulated. We note that the SCF theories[20,52,53] predict $d_l \propto N^{2/3}\chi^{1/6}$. The N scaling is confirmed in the figure. For large $\tilde{\epsilon}$ the chains are highly stretched. As seen below the AB junctions are confined to an almost microscopically thin interface. Thus, further increase in the repulsive energy between the two

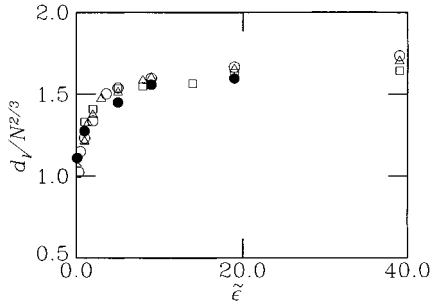

Figure 8. Equilibrium lamellar spacing d_l scaled by $N^{2/3}$ as a function of the excess AB interaction parameter $\tilde{\epsilon}$, for N = 40 (△), 100 (○), 200 (□), and 400 (●).

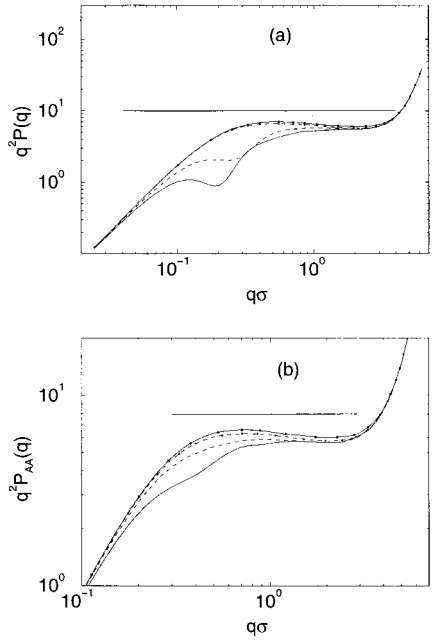

Figure 9. (a) Kratky plot of the single chain form factor $P(q)$ for two lamellar N = 200 systems: $\tilde{\epsilon}$ = 0.2 (dashed curves) and $\tilde{\epsilon}$ = 9.0 (solid curves). The curves with small circles are for wave vectors oriented in the lamellar planes, while the curves without symbols are for wave vectors perpendicular to the lamellae. The horizontal line indicates the slope expected for Gaussian chains. (b) Same quantities except that the form factor $P_{AA}(q)$ is for the A monomers only. Both the horizontal and the vertical scales are expanded to emphasize the differences between the curves.

species affects d_l only weakly, resulting in the leveling off of the plot. In this regime χ is no longer proportional to $\tilde{\epsilon}$ as discussed in the previous section.

Another interesting way to demonstrate the chain stretching is by plotting the average single chain form factor $P(q)$ defined as

$$P(q) = \frac{1}{N}\langle \sum_{ij} e^{i\mathbf{q}\cdot\mathbf{r}_{ij}} \rangle \tag{11}$$

averaged over different orientations of **q**. The sum is over all pairs in a single chain. The average is over all the chains in the system and over different times. A similar quantity $P_{AA}(q)$ is defined by summing only over pairs of monomers which are both species A. Figure 9a shows $P(q)$ for **q** vectors in the lamellar plane and perpendicular to it for two systems with N = 200. One of the systems $\tilde{\epsilon}$ = 0.2, is close to the ODT, while the other, $\tilde{\epsilon}$ = 9.0, is in the strong segregation limit. For **q** vectors in the lamellar plane, $P(q)$ of both systems only slightly deviate from the q^{-2} behavior, corresponding to that of Gaussian chains. Similar behavior is observed for $P(q)$ in the disordered phase near the ODT, where $P(q) \simeq q^{-a}$ with an effective exponent $a \simeq 2.15$. However, for **q** vectors perpendicular to the lamellar plane, a minimum appears, whose depth is significantly larger for the higher $\tilde{\epsilon}$ system. The curve for the intermediate ($\tilde{\epsilon}$ = 1.0) system, not shown on the plot for the sake of clarity, has a minimum of intermediate depth. The position q_m at which this minimum appears corresponds to a linear size $2\pi/q_m$. This size increases with increasing $\tilde{\epsilon}$. For the system with $\tilde{\epsilon}$ = 9.0, the minimum is quite well defined and occurs at $q_m = 0.23\sigma^{-1}$, corresponding to a size of 24.3σ. This is of the same order as the average end-to-end dimensions of the chain. The appearance of such a minimum is reminiscent of an elongated object of distinct boundaries. From the form factor $P_{AA}(q)$ of only the A parts of the chain (Figure 9b), one again sees a difference between wave vectors in the lamellar plane and in the perpendicular direction, with both deviating from a Gaussian behavior. Thus it seems that the stretching of the chains occurs both as a result of distortion of each subchain and from the separation of the subchains due to the interaction.

C. Concentration Profiles. Now we consider the ordering within the lamellar phases. To that end, we calculate the density profile of both A and B monomers along the z axis (perpendicular to the lamellar plane). This is done by dividing the z axis from $z/L_\perp = 0$ to 1 into small bins (of size 0.01) and keeping track of the number of A and B monomers in each bin. This number is calculated for a given system configuration and averaged over a large number of configurations. To account for the fact that the white noise term in the equation of motion introduces a center of mass motion of the whole system, we first remove this motion from the coordinates of all the monomers before calculating the density profile.

Figure 10a shows the density profiles of both types of monomers for the system with 200 chains of length N = 100 near the ODT ($\tilde{\epsilon}$ = 0.3). The density of either type of monomer never vanishes, so that there are no pure A or pure B domains in this system. Also shown in the figure are the density profiles of the free A and B end monomers and of the junction point. These are calculated in the same way as the overall density profiles, except that the sums include only the monomers at the free ends or the junction points, respectively. These show that even the free A ends have a finite density within the predominately B domains. The junction points are also to be found everywhere within the lamellae and are not constrained to a small interface region for this case which is in the weak segregation regime.

As $\tilde{\epsilon}$ is increased, the system becomes much more segregated, as seen in Figure 10b for $\tilde{\epsilon}$ = 1.0. Here the lamellae have regions which exclusively contain monomers of one type. However, the free ends still probe all the region accessible to monomers of the same type; that is, the density profile of the free ends vanishes only at those values of z where the overall density profile of the monomers of the same type vanish. Although the junction points are now more localized, they still probe a large volume. The width of the distribution function is about five monomer units. Monolayer interfaces are obtained only for larger values of $\tilde{\epsilon}$, as will be demonstrated below. These results agree with SCF theory.[22]

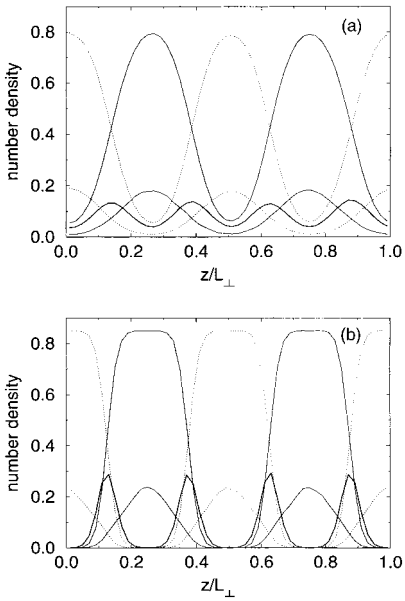

Figure 10. The number density of monomers of type A (the tall solid line) and of type B (the tall dotted line) for a system of 200 chains of length $N = 100$ at $\tilde{\epsilon} = 0.3$ (a) and 1.0 (b). $L_\perp = 44.1\sigma$. The density due to the end monomers of the two types (at the free ends of the chains) are shown as the lower full and dotted lines, respectively. The thick line shows the density of the junction points. The last three curves are multiplied by 10 for the sake of clarity.

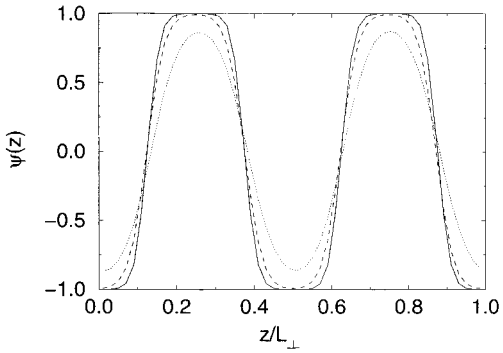

Figure 11. The order parameter for three $N = 100$ systems: $\tilde{\epsilon} = 1.0$ (solid line), 0.5 (dashed line), and 0.3 (dotted line).

The width of the interface can be quantified from the variation of the order parameter $\psi(z)$

$$\psi(z) = (\phi_A(z) - \phi_B(z))/(\phi_A(z) + \phi_B(z)) \qquad (12)$$

This function for $N = 100$ and for three values of $\tilde{\epsilon}$ is shown in Figure 11. The width of the interface region increases with decreasing $\tilde{\epsilon}$. To measure this width, we fit the interface width w to the form

$$\psi(z) = \tanh[2(z - z_I)/w] \qquad (13)$$

Here z_I is a point at which the order parameter vanishes. Fitting the order parameter around z_I to this functional form, we obtain estimates for the interface width, shown in Figure 12. It is tempting to associate w with the interfacial width of the interface. However, this averaging of the profile incorporates the effect of the intrinsic interfacial width w_o as well as other perturbations broadening the interface, such as capillary waves. To separate both effects uniquely, a systematic study of the interfacial profile for different system sizes would be needed. Since this is prohibitive

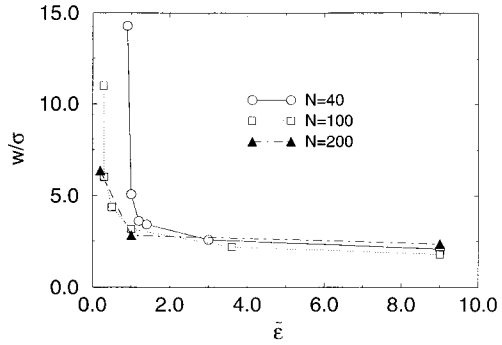

Figure 12. The width of the AB interface as a function of $\tilde{\epsilon}$ for systems of length $N = 40$, 100, and 200. The width is determined from fitting the order parameter to the functional form of eq 13. The lines are a guide to the eye only.

in terms of cpu time at this time, we instead estimate the relative contributions of the two contributions to w based on prior work on the interface between immiscible blends for the same model.[57] In capillary wave theory,[58] the roughness of the zero of a sharp interface $z_o(x,y)$ in the linearized regime of small distortions is given by

$$\langle(\Delta z_o)^2\rangle = \frac{k_B T}{2\pi\gamma} \ln\left(\frac{q_{max}}{q_{min}}\right) \qquad (14)$$

where γ is the interfacial tension between immiscible homopolymers and q_{min} and q_{max} are the minimum and maximum wave vectors of the fluctuations. For a polymer blend in which the interfaces are far apart, q_{min} is set by the lateral dimension of the interface $L_{||}$ and generally taken to be $\pi/L_{||}$. The upper cutoff q_{max} is usually assumed to be driven by some correlation length such as $\pi/(c'w_o)$, where c' is a number on the order of unity. However for lamellar diblocks the fluctuations are reduced due to the presence of nearby interfaces. Semenov[59] suggests that the lamellar spacing d_l sets the scale for q_{min}. Lacasse *et al.*[57] derived a general and formal argument to add the roughening effect of capillary waves to the intrinsic interfacial width. They find that

$$\Delta^2 = \Delta_o^2 + \frac{k_B T}{2\pi\gamma} \ln\left(\frac{\pi}{c q_{min} \Delta_o}\right) \qquad (15)$$

where Δ^2 measures the total interfacial width and Δ_o^2 is related to w_o^2. This equation is quite general and does not rely on any specific functional form to fit the interface. If one uses eq 13 to fit the profile, then $\Delta^2 = \pi^2 w^2/48$.

Using the values of the interfacial tension measured by Lacasse *et al.*[57] in their studies of the interface between symmetric blends, we can estimate the two contributions to Δ. Using these results and setting $q_{min} = \pi/d_l$ as suggested by Semenov[59] and $c \simeq 13$,[57] we find that the intrinsic width w_o dominates over the capillary contributions for the systems studied here. An interesting future study is to vary the size of the simulation cell and measure w to check these assumptions.

For high $\tilde{\epsilon}$, the width is small, and is of order monomer size. It is also independent of the chain length, in accordance with the SSL theories.[18−20] This is reasonable, since in this case the junction point is not influenced by the length of the chain, which is already highly stretched. The interface thickness for $N = 40$ and 100 systems increase slightly as $\tilde{\epsilon}$ is reduced down to

about its ODT value, at which point it increases sharply. It is hard to determine where this increase occurs for $N = 200$ due to the small number of data points; we expect the interface for this chain length to increase only mildly approaching $\tilde{\epsilon} = 0.2$, where the system is very close to the ODT and increase steeply only for lower values of $\tilde{\epsilon}$.

Anastasiadis *et al.*[60] and Mayes *et al.*[61] have studied the chain configurations in ordered symmetric PS−PMMA diblocks by neutron reflectivity. By selective labeling, they determined the monomer density profiles for each of the two blocks[60] as well as the center and end monomers.[61] Their results are qualitatively similar to our profiles. Far from the ODT, Mayes *et al.* find that the center junctions are pinned to the interface but the ends are well distributed throughout their respective domains. Anastasiadis *et al.* fit their profiles to several functional forms and found a hyperbolic tangent form to describe the interface adequately. We also have found this functional form satisfactory enough to calculate interface thicknesses. Anastasiadis *et al.* found that the interface width was independent of the distance from the ODT. We, however, find that the interface width is strongly dependent on the distance from the ODT. The change in the interface thickness with the degree of segregation, as seen in our simulations is also in qualitative agreement with the SCF theory calculations of Matsen and Bates[24] in the intermediate segregation regime.

IV. Diffusion

The diffusion coefficient of a chain in each of the three Cartesian directions is calculated from the long time behavior of the motion of its center of mass, $g_3(t)$. The components of $g_3(t)$ are defined by

$$g_{3\alpha}(t) = \langle [r_{cm\alpha}(t) - r_{cm\alpha}(0)]^2 \rangle \tag{16}$$

with $\alpha = x$, y, or z. Here $r_{cm\alpha}(t)$ are the components of the center of mass of a chain and $\langle \cdots \rangle$ denotes both an ensemble average over all chains and over many different starting states. At long times, $g_{3\alpha}(t) \rightarrow 2D_\alpha t$. Since our lamellae are oriented (by construction) in the xy plane, the diffusion constant in the lamellar plane is given by $D_{||} = (D_x + D_y)/2$, while perpendicular motion is characterized by $D_\perp = D_z$. The motion in the lamellar plane is given by

$$g_{3||}(t) = g_{3x}(t) + g_{3y}(t) \tag{17}$$

In the one phase region, the isotropic diffusion constant D decreases with increasing interaction strength $\tilde{\epsilon}$, as shown in Figure 13. Here D is the average of the three values of D_α, though the runs are sufficiently long that the differences in the three values are quite small. We denote the value for the homogeneous melt ($\tilde{\epsilon} = 0$) as D_0. For very short chains, $N = 10$ and 20, the chains show Rouse-like scaling for small $\tilde{\epsilon}$. However as $\tilde{\epsilon}$ increases the chains become stretched and the diffusion data, even for these very short chains, begin to deviate from the Rouse scaling $D \propto N^{-1}$. As N increases to 40, there is already some signature of a crossover to slower dynamics even for $\tilde{\epsilon} = 0$.[46,47] This crossover to slower diffusion becomes enhanced as $\tilde{\epsilon}$ increases. Hoffmann *et al.*[16] found using Monte Carlo simulations of symmetric diblock copolymers in the one phase region that $D(\tilde{\epsilon})/D(0)$ scales with $\tilde{\epsilon}N^\kappa$, with an effective exponent κ $\simeq 0.7$. As seen from Figure 13, the effective exponent κ would have to be much larger in order to scale our data. A value of $\kappa \simeq 1.5$ works reasonably well though it is not clear why the scaling exponent for the diffusion should be so large. Hamersky *et al.*[33] also found for short PS−PI diblocks that the diffusion constant does not obey simple Rouse scaling.

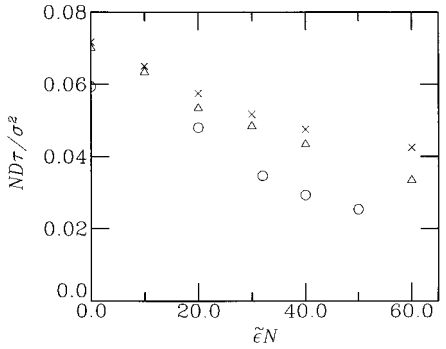

Figure 13. Diffusion constant D in the disordered phase for $N = 10$ (×), 20 (△), and 40 (○).

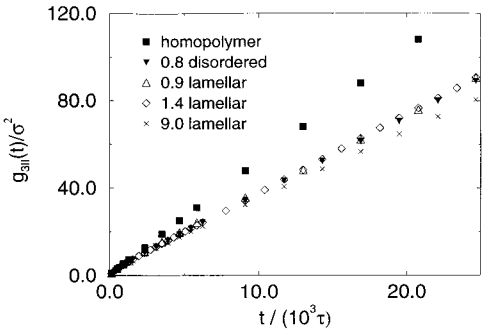

Figure 14. $g_{3||}(t)$ in the lamellar phase for $N = 40$ as a function of time for various values of $\tilde{\epsilon}$, indicated in the legend. Also shown are the same quantities for an homogeneous melt and a disordered system near the ODT.

In the lamellar phase, the shortest chain system we studied was $N = 40$, which is expected to obey Rouse dynamics. Figure 14 shows the behavior of $g_{3||}(t)$ as a function of time, for various values of the interaction parameter for $N = 40$. The figure includes curves for several lamellar systems, as well as for the isotropic homopolymer and for isotropic diblock near ODT (the system with $\tilde{\epsilon} = 0.8$). In these later two cases, we plot the motion in two directions, $g_{3x}(t) + g_{3y}(t)$ for comparison. The corresponding $D_{||}$ are calculated from the slope of the curves in the diffusive regime. From log−log plots of the same data (not shown) the regime in which $g_{3||}(t)$ depends linearly on t is reached rather quickly, within about 1000τ, allowing rather accurate determination of $D_{||}$.

The motion of the center of mass of the chain in the direction perpendicular to the lamellar layers is shown in Figure 15 for $N = 40$. Contrary to the case of lateral diffusion, here one sees a dramatic decrease in the diffusion constant with increasing $\tilde{\epsilon}$. For $\tilde{\epsilon} \gtrsim 1.4$, $g_{3\perp}(t)$ practically saturates at a constant value, corresponding roughly to the square of the thickness of the interface. For such cases, $D_\perp$ is too small for us to measure without prohibitively long runs. For small $\tilde{\epsilon}$, results for $D_\perp$ can be fit to an exponential decay, $D_\perp/D_0 = 0.57 \exp[-6.4(\tilde{\epsilon} - 0.85)]$. Here D_0 is the diffusion constant of the homogeneous melt. Following the motion of the center of mass of a single chain in the perpendicular direction, we observe that this motion is not smooth. Rather, the

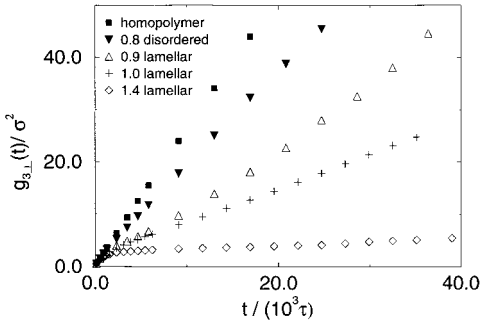

Figure 15. The perpendicular component of $g_3(t)$ in the lamellar phase for $N = 40$ as a function of time for various values of $\tilde{\epsilon}$. Also shown are the same quantities for an homogeneous melt and a disordered system at the ODT.

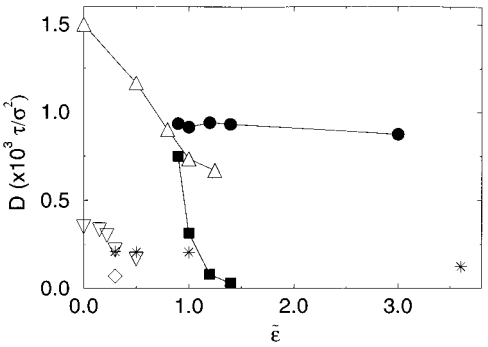

Figure 16. Diffusion coefficients as a function $\tilde{\epsilon}$: $D_{||}$ (●) and $D_\perp$ (■) for $N = 40$ lamellar, isotropic D (△) for disordered $N = 40$ melt, $D_{||}$ (∗) and $D_\perp$ (◇) for $N = 100$ lamellar, and isotropic D (▽) for disordered $N = 100$ melt. The lines for the $N = 40$ systems are only a guide to the eye.

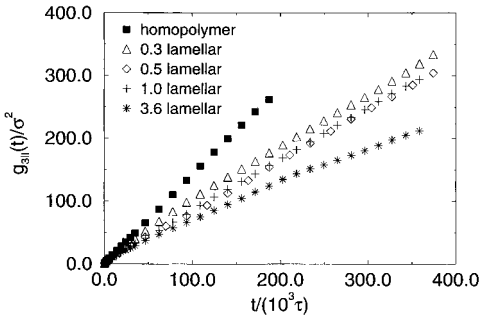

Figure 17. $g_{3||}(t)$ in the lamellar phase for $N = 100$ as a function of time for various values of $\tilde{\epsilon}$, indicated in the legend. Also shown is the same function for an homogeneous melt.

chain typically makes several attempts to move from one layer to another before it finally crosses.

The results for all the measured diffusion constants for $N = 40$ are presented in Figure 16. We find for the homogeneous system an isotropic diffusion constant $D_0 = 1.5 \times 10^{-3}\sigma^2/\tau$. Near the ODT D drops to $8.6 \times 10^{-4}\sigma^2/\tau$, about 40% lower than the diffusion constant in the homopolymer. For the lamellar system closest to the ODT (the system with $\tilde{\epsilon} = 0.9$), $D_{||} = 9.5 \times 10^{-4}$, slightly higher than the diffusion constant in the isotropic phase near ODT. In the lamellar phase, $D_{||}$ does not vary very much with increasing $\tilde{\epsilon}$. Even for $\tilde{\epsilon} = 9.0$ (but shown in Figure 16), which is deep in the strong segregation regime ($N\tilde{\epsilon} = 360$), $D_{||}$ decreases only to $8.0 \times 10^{-4}\sigma^2/\tau$.

Results for $g_{3||}(t)$ for four values of $\tilde{\epsilon}$ are compared to that for a homopolymer ($\tilde{\epsilon} = 0$) for $N = 100$ in Figure 17. Similar to the shorter chains, the changes in the slope of the curves with increasing $\tilde{\epsilon}$ are insignificant.

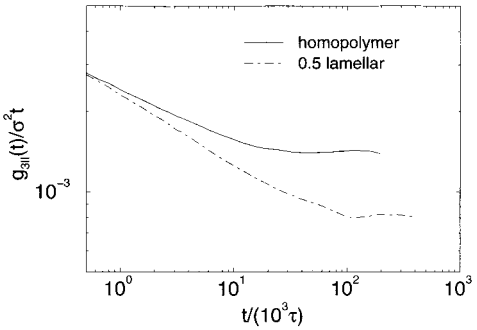

Figure 18. $g_{3||}(t)/t$ for a homopolymer melt with $N = 100$, and for the lamellar system with $\tilde{\epsilon} = 0.5$. The flatting of the curves at late times indicates the transition to the diffusive regime.

All the measured diffusion constants for $N = 100$ from our simulations are also shown in Figure 16. For $N = 100$, the homogeneous diffusion constant is $3.5 \times 10^{-4}\sigma^2/\tau$. The isotropic diffusion constant of the disordered phase decreases with increasing $\tilde{\epsilon}$, and reaches a value of about $2.1 \times 10^{-4}\sigma^2/\tau$ at the ODT. This corresponds to a decrease of about 60%, similar to the decrease in the $N = 40$ systems. The parallel diffusion constant in the lamellar phase closest to the ODT is almost indistinguishable from the one in the disordered phase. At higher values of $\tilde{\epsilon}$, $D_{||}$ decreases only slightly. At $\tilde{\epsilon} = 3.6$, corresponding to $N\tilde{\epsilon} = 360$, $D_{||}$ decreases to $1.3 \times 10^{-4}\sigma^2/\tau$, lower only by 40% from the value at the ODT. Perpendicular diffusion was observed for $N = 100$ only for $\tilde{\epsilon} = 0.3$. For this system, $D_\perp$ was found to be $0.65 \times 10^{-4}\sigma^2/\tau$. The ratio $D_\perp/D_{||}$ at the ODT is then about $^1/_3$, significantly lower than the ratio of 0.8 for $N = 40$ systems. No measurable perpendicular motion could be observed in systems with higher $\tilde{\epsilon}$.

These results on diffusion in the lamellar planes confirm the Barrat−Fredrickson prediction that in a system of Rouse chains (with no entanglements), the parallel diffusion is unaffected by the amplitude of the chain stretching. Our results for $N = 40$ clearly show that $D_{||}$ is practically constant from the ODT ($N\tilde{\epsilon}_{ODT} \simeq 34$) all the way up to highly stretched chains with $N\tilde{\epsilon} = 360$. The situation is rather similar in $N = 100$ systems. The decrease in $D_{||}$ from near ODT to the system with $N\tilde{\epsilon} = 360$ is about 40% only.

One effect of the chain stretching on parallel diffusion is on the time scale at which diffusive motion sets in. Only when the center of mass of the chain has moved a distance comparable to R_G, the motion becomes diffusive, $g_3(t) \propto t$. Figure 18 shows $g_{3||}(t)/t$ for a homopolymer melt and a lamellar system with $\tilde{\epsilon} = 0.5$. It is clearly seen that the transition to diffusive regime occurs considerably later for the lamellar system than for the homopolymer. Such delay is present to a lesser degree in $N = 40$ systems. For $N = 200$, this delay is much more prominent, and is the reason why we could not measure $D_{||}$ for the lamellar systems within reasonable simulation times, although runs of comparable length were sufficient to measure D_0 for the homopolymer melt.[46,62]

Theoretical treatment by Barrat and Fredrickson[25] estimates that for Rouse chains, the diffusion constant in the direction perpendicular to the lamellar plane near ODT will be lower by not more than 40% compared to the isotropic diffusion constant in the disordered phase at ODT. Our results for $N = 40$ are clearly consistent with this prediction. For the $N = 100$ system near the ODT (system with $\tilde{\epsilon} = 0.3$), we found a more significant

reduction (about 70%). This is probably due to the fact that chains of length 100 monomers are above the entanglement length, and cannot be considered as perfect Rouse chains any more. Barrat and Fredrickson also predict that with increasing χN the perpendicular diffusion constant should decrease exponentially with χN, in agreement with the results given for $N = 40$ in Table 2.

Of the three $N = 200$ systems, only the one with $\tilde{\epsilon} = 0.2$ exhibited a measurable diffusive motion. For this system, which is closest to the ODT, $D_{||}$ is about $4.9 \times 10^{-5}\sigma^2/\tau$. However, even after $t = 3.0 \times 10^5\tau$, $g_{3||}(t) \approx 90\sigma^2$, not much larger than $\langle R_G^2 \rangle$. Therefore, the system has barely entered the diffusive regime, and the diffusion constant derived is not very reliable. The perpendicular motion is too slow to determine $D_\perp$. For higher values of $\tilde{\epsilon}$, all the components of $g_3(t)$ reach values considerably smaller than $\langle R_G^2 \rangle$, with the motion being in the sub-diffusive regime even at the longest times simulated. Therefore we could not derive any diffusion constants for these systems.

V. Entanglement Effects

In our previous letter,[26] we found that the slowing down for short times results from the "caging" of each chain within the volume formed by the surrounding chains. Here we present additional evidence for the reduction of entanglement density compared to homopolymer melts.

Reduced diffusion constants compared to an isotropic melt can be for a variety of reasons. One would be an increased monomeric friction constant of the monomers. This would just shift the mean square displacements but not alter the power laws. The other would be a caging effect on the overall chain as a consequence of the smectic structure of the layers. To understand the origin of this reduced diffusion in ref 26, we followed the motion of the individual monomers by measuring the separate Cartesian components of the mean squared displacement of monomer k, given by

$$g_{1\alpha}^{(k)}(t) = \langle [r_{k,\alpha}(t) - r_{k,\alpha}(0)]^2 \rangle \tag{18}$$

We observed that the transition to the diffusive regime in the lamellar phase takes place significantly later as $\tilde{\epsilon}$ and/or the chain length increases. We observed an increased local friction of the monomers located near the interface. More interestingly we observed a drop in the slope (on the log−log plot) of $g_{1||}(t)$ for the lamellar cases before the t^1 regime sets in. This slowing down is reminiscent of a caging effect, imposed by other stretched chains on the motion of a given chain. As a result, diffusive motion is delayed even further and the drop in the magnitude of $g_{1||}(t)$ becomes more pronounced.[26]

We did not observe such an amplitude drop in $g_{1||}(t)$ for the outer monomers at short times since these beads experience only a homogeneous environment of like monomers. However, for later times a similar delay is observed, as the outer monomers eventually have to follow the slow motion of the inner ones. Therefore the center of mass motion, which averages the behavior of all the monomers, exhibits an overall delay in crossing over to the diffusive regime, with increasing $\tilde{\epsilon}$. This caging effect is not to be confused with the reptation induced by entanglements in the homopolymer case, as was done in ref 37. The slowing down is mainly determined by the confinement of the middle part of the chain to the interface, but not due to entanglements. The reduction of the entanglement density can be estimated by the chains which interpenetrate. In a homopolymer melt the volume of each chain is shared by $O(N^{1/2})$ other chains, giving rise to $O(N)$ topological constraints. Employing scaling arguments for the elongated chains would even suggest a smaller N dependency for the chain−chain interpenetration. A first estimate of the chain overlap is the number of distinct contacts, meaning the number of different chains which touch the test chain, within a lamella (contacts between different lamellae are not relevant). In the strongly segregated regime about 22 ($N = 100$), 30 ($N = 200$), and 35 ($N = 400$) distinct chain contacts occur, significantly below the homopolymer result (about 30 for $N = 100$ and above 50 for $N = 350$).

The motion of a chain inside its cage is best demonstrated by visualization of the primitive chain (PC),[46] which can be constructed by continuously coarse graining along the chain. In this procedure we subdivide the chain into $N_p = (N + 1 - N_c)$ subunits. The position of the new monomers is given by

$$\mathbf{R}_k = \frac{1}{N_c} \sum_{i=k}^{k+N_c-1} \mathbf{r}_i \tag{19}$$

This coarse graining is useful since it eliminates some of the thermal fluctuations and allows one to visualize the motion of the chain along its tube, if present. Here, we take $N_c = N_e = 35$. In our earlier studies of the dynamics of homopolymer melts,[46,47] following the motion of the inner monomers of the PC was very useful in demonstrating that the chain is confined to a tube.

Figures 19 and 20 show the time evolution of the PC for a $N = 400$ diblock in the strongly and weakly segregated regimes, respectively. Note that as expected from the previous analysis of the interface width, the center monomers remains very near the interface in the strong segregation limit (Figure 19), while in the weak segregation limit (Figure 20), the central monomer wanders quite far from the interface. The reptation tube diameter obtained from the homopolymer melt is indicated. For the time covered, the conformations in a homopolymer melt would stay within a region of the width of the tube diameter d_T, diffusing up and down the tube. Here, however, we have a clear confinement of the center monomers to the interface, and the overall motion of the chain parallel to the interface exceeds the homopolymer tube diameter in the strong segregation limit. If the entanglement density were not reduced, the position would be confined to an area given by $d_T^2 \approx 22\sigma^2$, as found in the case of e.g. entangled polymer networks. Here we find $g_{1||}(t) \simeq 47\sigma^2$ and $56\sigma^2$ and $g_{1\perp}(t) \simeq 1.7\sigma^2$ and $1.8\sigma^2$ for the middle monomers at $t = 100000\tau$ and 200000τ, respectively, in the strongly segregated regime ($\tilde{\epsilon} = 9.0$) compared to homopolymer melt where we find $g_1(t) \simeq 80\sigma^2$ and $105\sigma^2$, dominated by motion along the tube, for the same times. In the weakly segregated regime ($\tilde{\epsilon} = 0.1$), $g_{1||}(t) \simeq 46\sigma^2$ and $50\sigma^2$ and $g_{1\perp}(t) \simeq 32\sigma^2$ and $34\sigma^2$ for the middle monomers at $t = 100000\tau$ and 200000τ, respectively. A chain in the isotropic melt moves only somewhat farther than a chain in weak segregated regime during this time regime. Both move considerably farther than for a chain in the strong segregation regime. The motion of center beads for chains in the strongly segregated regime are clearly confined to the $2-d$ interface as seen from the

Figure 19. Visualization of the time evolution of a single primitive path constructed from block copolymer of $N = 400$ and $\tilde{\epsilon} = 9.0$ with $N_c = 35$. The system is in the strongly segregated regime. The tube diameter $d_T \approx 5\sigma$, as found in the homopolymer melts, is indicated by the black bar. The total time of the run is 200000τ with an increment of 6500τ between the different conformations shown. The cell which is plotted here is only a fraction of the full simulation cell. The dimensions of the cell here and in the next figure are $L_\perp = 60.0\sigma$ and $L_\parallel = 30.0\sigma$.

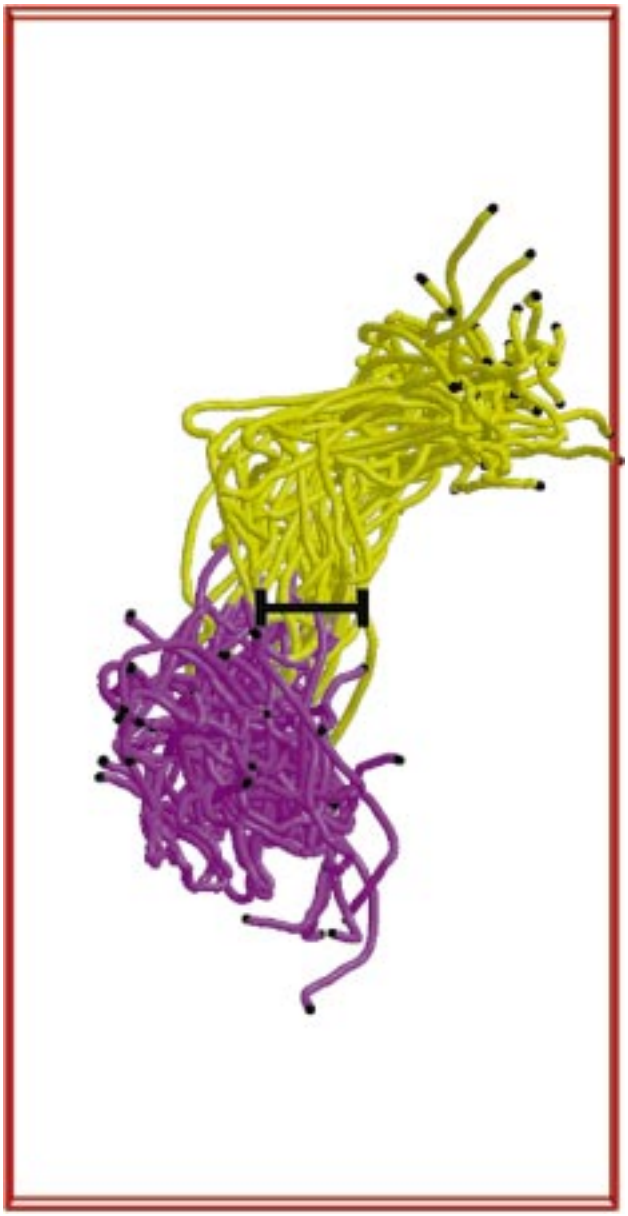

Figure 20. Visualization of the time evolution of a single primitive path constructed from block copolymer of $N = 400$ and $\tilde{\epsilon} = 0.1$. The remaining details are the same as Figure 19.

very small values for $g_{1\perp}(t)$. Whether this continues for the present N, or is just a signature of a reduced entanglement density, can only be revealed by further investigations.

A very stringent and direct test of the reptation concept is to identify the motion along the contour directly. Following the procedure described in ref 46, we subdivided the motion of monomers in the PC along the contour, $\tilde{g}_\parallel(t)$, and perpendicular to the contour $\tilde{g}_\perp(t)$ for each monomer k. For $\tilde{g}_\parallel(t)$ we explicitly construct the motion along the primitive path, while $\tilde{g}_\perp(t)$ measures the minimal distance for monomer k from anywhere along the primitive path. For an infinite reptating chain, $\tilde{g}_\perp(t)$ should be a constant while $\tilde{g}_\parallel(t)$ should follow the Rouse diffusion along the contour and thus follow a $t^{1/2}$ law up to the Rouse time of the inner monomers. Figure 21 shows the ratio of these two quantities for the two $N = 400$ lamellar systems and for a homopoly-

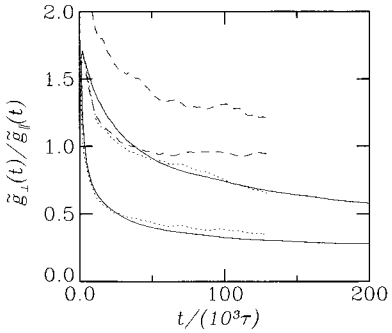

Figure 21. $\tilde{g}_\perp(t)/\tilde{g}_\parallel(t)$ for the inner monomer (lower curve) and the tenth monomer (upper curve) of the primitive chain constructed using $N_c = 35$. Results are shown for $N = 400$ for $\tilde{\epsilon} = 0.1$ (short dashed lines) and $\tilde{\epsilon} = 9.0$ (long dashed lines) and for a homopolymer melt ($\tilde{\epsilon} = 0.0$) for $N = 350$ (solid lines).

mer melt of $N = 350$ chains.[62] Note that the results for the homopolymer and the weakly segregrated case are nearly identical. The motion of the chains is strongly confined to the tube. This is in contrast to the motion for the strongly segregated regime in which the motion for center monomers is equal parallel and perpendicular to the tube. This supports our earlier findings that strong chain stretching reduces the entanglements in lamellar systems, compared to isotropic melts. At least for the time regimes studied for chains of length $N =$ 200 and 400, the chains in the strongly stretched regime move more like soft elipsoids. We see no evidence for a block-retraction mechanism though this mechanism may play a role for long chains and/or longer times. For these relatively early times, the motion in the strongly segregated regime is dominated by the confinement of the center to a nearly $2-d$ interface. In the weak segregation regime, at least for short times, the motion is strongly confined to a tube as in a homopolymer melt, since the middle monomer connecting the two blocks is not confined to the interfacial regime as seen in Figure 10.

VI. Summary and Conclusions

In this paper, we have presented our continuum space simulations of symmetric diblock copolymers, both in the disordered and the lamellar phases. For the lamellar systems, we have used constant pressure simulations in order to determine the equilibrium lamellar spacing, so that the dimensions of the simulation cell are commensurate with the lamellar spacing. We have studied both equilibrium properties and diffusion behavior in both phases, using chains of length $N = 10$ to 400.

For disordered systems, the non-Gaussian character of the chains is demonstrated. We also show that the characteristic wavelength of the density fluctuations increases as the ODT is approached. The functional form of the structure factor corresponding to these fluctuations is shown to be consistent with the predictions of Leibler[6] and Fredrickson and Helfand.[7] The lamellar ordering within the ordered phase is quantitatively described and compared with theoretical and experimental results. The changes in the chain conformations are found to be reflected in the single chain and single block (subchain) form factors. These indicate formation of a sticklike object with increasing AB interaction energy.

Our results for the self-diffusion constant D in the disordered phase decrease as the interaction strength $\tilde{\epsilon}$ increased as expected and are continuous through the order−disorder transition. We observe a stronger dependence of D on chainlength N than observed previously by Hoffmann *et al.*[16] In the lamellar phase, we find that, for short chains (of length $N = 40$ and 100), $D_{\|}$ below the ODT is essentially unaffected by chain stretching. This is in accordance with the Rouse-like motion of chains. Perpendicular diffusion is strongly suppressed by the lamellar structure. Our results are roughly consistent with ref 25. We find that the onset of diffusive motion is delayed with increasing AB interaction energy. This delay occurs for short chains as well, although it becomes emphasized for longer chains. We therefore could not measure the diffusion constants of longer chains ($N > 100$) within a reasonable simulation time. Observation of the motion of longer chains (N up to 400) indicates that strong chain stretching reduces the entanglements in lamellar systems, compared to isotropic melts.

Acknowledgment. We thank M. Pütz for help in the analysis of the primitive chain. This work as supported in part by the BMBF project "Computer Simulations of Complex Materials".

References and Notes

(1) Bates, F. S.; Fredrickson, G. H. *Annu. Rev. Phys. Chem.* **1990**, *41*, 525.
(2) Bates, F. S. *Science* **1991**, *251*, 898−905.
(3) Binder, K. *Adv. Polym. Sci.* **1994**, *112*, 181.
(4) Binder, K. In *Monte Carlo and Molecular Dynamics Simulations in Polymer Science*; Binder, K., Ed.; Oxford University Press: New York, 1995.
(5) Fredrickson, G. H.; Bates, F. S. *Annu. Rev. Mat. Sci.* **1996**, *26*, 503.
(6) Leibler, L. *Macromolecules* **1980**, *13*, 1602.
(7) Fredrickson, G. H.; Helfand, E. *J. Chem. Phys.* **1987**, *87*, 697.
(8) Stepanow, S. *Macromolecules* **1995**, *28*, 8233.
(9) David, E. F.; Schweizer, K. S. *J. Chem. Phys.* **1994**, *100*, 7767; **1994**, *100*, 7784.
(10) Guenza, M.; Schweizer, K. S. *J. Chem. Phys.* **1997**, *106*, 7391; *Macromolecules* **1997**, *30*, 4205.
(11) Schweizer, K. S.; Curro, J. G. In *Advances in Chemical Physics*; Prigogine, I., Rice, S. A., Eds.; Wiley: New York, 1997; Vol. 98.
(12) Guenza, M.; Tang, H.; Schweizer, K. S. *J. Chem. Phys.* **1998**, *108*, 1257. Guenza, M.; Schweizer, K. S. *J. Chem. Phys.* **1998**, *108*, 1271.
(13) Fried, H.; Binder, K. *Europhys. Lett.* **1991**, *16*, 237; *J. Chem. Phys.* **1991**, *94*, 8349.
(14) Grest, G. S.; Lacasse, M.-D.; Kremer, K.; Gupta, A. *J. Chem. Phys.* **1996**, *105*, 10583.
(15) Dotera, T.; Hatano, A. *J. Chem. Phys.* **1996**, *105*, 8413.
(16) Hoffmann, A.; Sommer, J.-U.; Blumen, A. *J. Chem. Phys.* **1997**, *106*, 6709.
(17) Almdal, K.; Rosedale, J. H.; Bates, F. S.; Wignall, G. D.; Fredrickson, G. H. *Phys. Rev. Lett.* **1990**, *65*, 1112.
(18) Helfand, E. *Macromolecules* **1975**, *8*, 552.
(19) Helfand, E.; Wasserman, Z. R. *Macromolecules* **1976**, *9*, 879.
(20) Semenov, A. N. *Sov. Phys. JETP* **1985**, *61*, 733.
(21) Shull, K. R. *Macromolecules* **1992**, *25*, 2122.
(22) Shull, K. R.; Mayes, A. M.; Russell, T. P. *Macromolecules* **1993**, *26*, 3929.
(23) Matsen, M. W.; Bates, F. S. *Macromolecules* **1996**, *29*, 1091.
(24) Matsen, M. W.; Bates, F. S. *J. Chem. Phys.* **1997**, *106*, 2436.
(25) Barrat, J.-L.; Fredrickson, G. H. *Macromolecules* **1991**, *24*, 6378.
(26) Murat, M.; Grest, G. S.; Kremer, K. *Europhys. Lett.* **1998**, *42*, 401.
(27) Leibig, C. M.; Fredrickson, G. H. *J. Polym. Sci., B: Polym. Phys.* **1996**, *34*, 163.
(28) Tang, H.; Schweizer, K. S. *J. Chem. Phys.* **1995**, *103*, 6296.
(29) Shull, K. R.; Kramer, E. J.; Bates, F. S.; Rosedale, J. H. *Macromolecules* **1991**, *24*, 1383.
(30) Fleischer, G.; Fujara, F.; Stühn, B. *Macromolecules* **1993**, *26*, 2340.
(31) Dalvi, M. C.; Eastman, C. E.; Lodge, T. P. *Phys. Rev. Lett.* **1993**, *71*, 2591.
(32) Ehlich, D.; Takenaka, M.; Okamoto, S.; Hashimoto, T. *Macromolecules* **1993**, *26*, 189; Ehlich, D.; Takenaka, M.; Hashimoto, T. *Macromolecules* **1993**, *26*, 492.
(33) Hamersky, M. W.; Tirrell, M.; Lodge, T. P. *Langmuir* **1998**, *14*, 6974.
(34) Dalvi, M. C.; Lodge, T. P. *Macromolecules* **1993**, *26*, 859.
(35) Lodge, T. P.; Dalvi, M. C. *Phys. Rev. Lett.* **1995**, *75*, 657.
(36) Colbyy, R. H. *Curr. Opin. Colloid Interface Sci.* **1996**, *1*, 454.
(37) Pan, X.; Shaffer, J. S. *Macromolecules* **1996**, *29*, 4453.
(38) Pakula, T.; Karatasos, K.; Anastasiadis, S. H.; Fytas, G. *Macromolecules* **1997**, *30*, 8463.
(39) Pakula, T. *Macromolecules* **1987**, *20*, 679.
(40) Carmesin, I.; Kremer, K. *Macromolecules* **1989**, *21*, 2819.
(41) Hoffmann, A.; Sommer, J.-U.; Blumen, A. *J. Chem. Phys.* **1997**, *107*, 7559.
(42) Haliloğlu, T.; Balaji, R.; Mattice, W. L. *Macromolecules* **1994**, *27*, 1473.
(43) Kikuchi, M.; Binder, K. *Europhys. Lett.* **1993**, *21*, 427.
(44) Larson, R. G. *Macromolecules* **1994**, *27*, 4198.
(45) Larson, R. G. *Mol. Simul.* **1994**, *13*, 321.

(46) Kremer, K.; Grest, G. S. *J. Chem. Phys.* **1990**, *92*, 5057.
(47) Kremer, K.; Grest, G. S. In *Monte Carlo and Molecular Dynamics Simulations in Polymer Science*; Binder, K., Ed.; Oxford University Press: New York, 1995.
(48) Grest, G. S.; Murat, M. In *Monte Carlo and Molecular Dynamics Simulations in Polymer Science*; Binder, K., Ed.; Oxford University Press: New York, 1995.
(49) Gehlsen, M. D.; Rosedale, J. H.; Bates, F. S.; Wignall, G. D.; Hansen, L.; Almdal, K. *Phys. Rev. Lett.* **1992**, *68*, 2452.
(50) Allen, M. P.; Tildesley, D. J. *Computer Simulation of Liquids*; Clarendon: Oxford, England, 1987.
(51) Parrinello, M.; Rahman, A. *Phys. Rev. Lett.* **1980**, *45*, 1196.
(52) Helfand, E.; Wasserman, Z. R. *Macromolecules* **1980**, *13*, 994.
(53) Ohta, T.; Kawasaki, K. *Macromolecules* **1986**, *19*, 2621.
(54) Bates, F. S.; Rosedale, J. H.; Fredrickson, G. H.; Glinka, C. J. *Phys. Rev. Lett.* **1988**, *61*, 2229.
(55) Bates, F. S.; Rosedale, J. H.; Fredrickson, G. H. *J. Chem. Phys.* **1990**, *92*, 6255.
(56) Minchau, B.; Dünweg, B.; Binder, K. *Polym. Commun.* **1990**, *31*, 348.
(57) Lacasse, M.-D.; Grest, G. S.; Levine, A. J. *Phys. Rev. Lett.* **1998**, *80*, 309.
(58) Buff, F. P.; Lovett, R. A.; Stillinger, F. H. *Phys. Rev. Lett.* **1965**, *15*, 621. Beysens, D.; Robert, M. *J. Chem. Phys.* **1987**, *87*, 3056. Semenov, A. N. *Macromolecules* **1994**, *27*, 2732.
(59) Semenov, A. N. *Macromolecules* **1993**, *26*, 6617.
(60) Anastasiadis, S. P.; Russell, T. P.; Satija, S. K.; Majkrzak, C. F. *J. Chem. Phys.* **1990**, *92*, 5677.
(61) Mayes, A. M.; Johnson, R. D.; Russell, T. P.; Smith, S. D.; Satija, S. K.; Majkrzak, C. F. *Macromolecules* **1993**, *26*, 1047.
(62) Dünweg, B.; Grest, G. S.; Kremer, K. In *Numerical Methods for Polymeric Systems*; Whittington, S., Ed.; Springer-Verlag, New York, 1998; Vol. 102, p 159.

MA981512P